IEEE Access
Multidisciplinary | Rapid Review | Open Access Journal

Received July 24, 2020, accepted August 1, 2020, date of publication August 4, 2020, date of current version August 17, 2020.

Digital Object Identifier 10.1109/ACCESS.2020.3014248

Impedance-Based Stability Analysis and Stabilization Control Strategy of MMC-HVDC Considering Complete Control Loops

TAIYUAN YIN[1], (Student Member, IEEE), YUE WANG[1], (Member, IEEE), BO YUE[2], PENGFAN XU[1], PENGKUN LI[1], NIAN MEI[2], AND DONG XU[2]

[1]State Key Laboratory of Electrical Insulation and Power Equipment, Xi'an Jiaotong University, Xi'an 710049, China
[2]State Grid Economic and Technological Research Institute, Beijing 102209, China

Corresponding author: Yue Wang (davidwangyue@mail.xjtu.edu.cn)

This work was supported by the Science and Technology Projects of State Grid Corporation of China (SGCC) under Grant 4000-201956494A-0-0-00.

ABSTRACT Impedance-based stability criterion is effective for analyzing the oscillation phenomenon in modular multilevel converter-based high-voltage DC (MMC-HVDC) transmission system, and modeling MMC impedance is the critical step. However, few papers have modeled MMC impedance with comprehensive consideration of time delay and outer-loop control at the same time. The stabilization strategies to improve system stability are not considered during impedance modeling, and the influences of stabilization strategy on impedance are not analyzed mathematically, either. In this article, an accurate sequence impedance model of MMC is derived with the consideration of time delay and complete control loops. Based on this impedance model, the negative damping caused by time delay is pointed out and the weak stability of grid-tied MMC system is analyzed. Then a stabilization control strategy is proposed to suppress the system oscillation. In the meantime, taking the proposed stabilization strategy into account, impedance modeling is revised to study the influence of this strategy on MMC impedance. Furthermore, based on this revised impedance model, an optimal design method for controller parameters of the stabilization strategy is proposed to maximize the phase margin of the interconnected system. Finally, the effectiveness of the accurate impedance model, the proposed stabilization control strategy and optimal design method are verified by simulation results.

INDEX TERMS Modular multilevel converter (MMC), impedance model, oscillation suppression, time delay, optimal design.

I. INTRODUCTION

Modular multilevel converter (MMC) has attracted a lot of research attention especially after the accomplishment of the Trans Bay Cable project in America [1]. Due to its advantages of modularity, low switching frequency and low distortion output voltage waveforms, MMC has been widely used in high-voltage direct current (HVDC) transmission system [2]–[4]. However, with the wide application of MMC-HVDC technology, its stability problems are increasingly prominent. A subsynchronous oscillation phenomenon was reported in MMC-HVDC for wind farm integration [5]. A resonance issue in North Sea offshore wind farm which uses MMC-HVDC transmission has been reported in [6]. It was also reported that a resonance occurred in Luxi back-to-back HVDC project in China [7].

Impedance based stability criterion is effective for analyzing practical resonance and control interaction problems for grid-connected converters [8]. In this approach, the converter system is decomposed into a positive-sequence and a negative-sequence subsystem, and the Nyquist stability criterion is applied to the grid-converter impedance ratio to determine the interconnected system stability [9]. To utilize impedance-based stability criterion for MMC-HVDC stability analysis, the most important prerequisite is to establish impedance model of MMC. Impedance modeling of MMC is

The associate editor coordinating the review of this manuscript and approving it for publication was Guangdeng Zong.

This work is licensed under a Creative Commons Attribution 4.0 License. For more information, see https://creativecommons.org/licenses/by/4.0/

much more complex than that of conventional voltage-source converters (VSCs) due to the complex internal dynamics of MMC.

Several average models have been proposed in [10]–[13], but internal dynamics of MMC such as capacitor voltage fluctuations and circulating currents are neglected. Reference [14] established MMC impedance models which treated all module capacitor voltages as constant and cannot accurately reflect the actual characteristics of the MMC. Impedance models of MMC considering its internal dynamics were established by multi-harmonic linearization [9], however, time delay and the outer-loop control were not considered. Harmonic state-space (HSS) modeling method was introduced to build the impedance models of MMC in [15], but the closed-loop control of MMC in [15] is direct three-phase voltage control, which is not common in practical projects.

The effect of time delay has been studied in the stability analysis of current control of grid-tied VSIs, which are mainly based on system loop gain and analysis of phase-lag influence, however, influence of delay on impedance characteristics are not shown [16], [17]. The influence of time delay on two-level voltage-source converter (VSC) impedance was studied in [18], however, the modeling of MMC is much more complex than that of VSC. Time delay was considered in [19], but specific modeling process was not expressed and outer-loop control was not considered. In practical HVDC projects, time delay of MMC is included in the procedures of data sampling, data fault tolerance processing in polar control (PC) system, digital processor computation in PC system, commands delivering process from PC system to valve base control (VBC) system, digital processor computation in VBC system and commands delivering process from VBC system to IGBTs. According to engineering experience of HVDC projects in China, the total delay is generally around 300μs, no more than 900μs, which is not small enough to be ignored. The instability of VSC caused by the delay has been analyzed in [16]–[18], and MMC is also very likely to be unstable due to time delay. Although MMC includes time delay and outer-loop control in practical conditions, most previous works ignored the time delay or outer-loop control during the modeling process, so impedance characteristics of MMC may not fully embodied.

The subsynchronous oscillation was suppressed by optimal design of controller parameters in [5], however, the influence of time delay was not discussed. An additional virtual parallel damping controller was proposed to suppress the oscillation of MMC-based DC-grid in [20], but the time delay was not considered, and the impedance model including this virtual damping controller was not established, either. Reference [21] proposed a harmonic elimination control strategy to mitigate the harmonic resonance in MMC-HVDC multiterminal systems, however, the influence of this harmonic elimination control strategy on impedance was not analyzed, and the parameters design of this control strategy was not mentioned, either. Some relevant nonlinear methods are applied to analyze the stability of switched system and improve its stability [22]–[24].

Based on the above analysis, a more accurate MMC impedance considering complete control loops and time delay is necessary to be established, and the corresponding influence of stabilization control strategy on impedance characteristics should be further analyzed.

In this article, an accurate sequence impedance model of MMC considering complete control loops is derived. Not only current inner-loop and circulating current control loop are considered, but also power outer-loop control, PLL, time delay and stabilization control are considered during modeling process. Based on this impedance model, the influences of parameters in different control loops and time delay on impedance characteristics are analyzed. The negative damping of impedance caused by time delay is pointed out and the weak stability of grid-connected MMC is analyzed. Then, a stabilization control strategy is proposed to suppress the system oscillation. In the meantime, taking the proposed stability strategy into account, impedance modeling is revised to study the influence of the proposed stabilization control strategy on MMC impedance. Furthermore, on the basis of revised impedance model considering stabilization strategy, an optimal design method for controller parameters of the stabilization control strategy is proposed to maximize the phase margin of the interconnected system. Finally, the correctness of the theoretical analysis, the effectiveness of proposed stabilization control strategy and optimal design method are verified by simulation results.

The main contribution of this article is summarized as: (1) an accurate impedance model of MMC is established with consideration of power outer-loop control, time delay and stabilization control strategy; (2) the negative damping of impedance caused by time delay is pointed out and analyzed; (3) an optimal design method for controller parameters of the stabilization control strategy is proposed.

The rest of this article is organized as follows: Section II presents the small signal model of MMC power stage. Section III derives the small signal mode of control stage. The small signal impedance model is validated, and the influences of different control loops and time delay are analyzed in Section IV. In Section V, the stability of MMC interconnected system is analyzed and a stabilization control strategy is proposed, meanwhile, the parameters of stabilization control strategy are designed optimally. Finally, the conclusion is shown in Section VI.

II. MMC POWER STAGE SMALL SIGNAL MODEL

MMC power stage small signal model is established based on harmonic linearization in this section.

Fig. 1 shows the circuit diagram of an MMC with voltage perturbation. It consists of six bridge arms, and each arm consists of N submodules and one arm inductor. SMi ($i = 1, \ldots$,n) is the ith submodule of each arm. And most electrical variables have two subscripts, respectively designates the phase (a, b and c) and the arm (u for the upper arm,

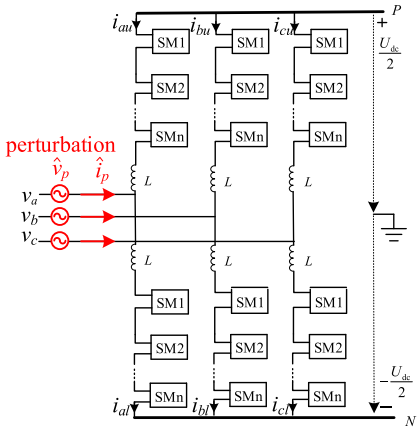

FIGURE 1. Diagram of MMC with AC side voltage perturbation.

and l for the lower arm). In addition, L is the inductance of the arm inductor and its equivalent parasitic resistance is r_L, C_m is the capacitance of the submodule capacitor.

The first step of modeling MMC sequence impedance by harmonic linearization is to add a sinusoidal voltage perturbation at frequency f_p to the AC side of MMC as shown in Fig. 1 [9]. In general, phase a voltage with a small voltage perturbation at frequency f_p can be written as [15]:

$$v_a(t) = V_a \cos(2\pi f_1 t) + \hat{V}_p \cos(2\pi f_p t + \varphi_p). \quad (1)$$

where V_a is the amplitude of grid voltage in phase a, $\hat{\mathbf{v}}_p$ and are ϕ_p the amplitude and phase of voltage perturbation. Phase b and c perturbations are defined similarly by adding $\pm 2\pi/3$ to the phase depending on the sequence of the perturbation.

Harmonic linearization method is a convenient method to capture the impedance of converters. The harmonic linearization method has several advantages, particularly compared to modeling in the dq-coordinate system: the steady-state operation trajectory can include any number of harmonics, and the calculated impedance has clear physical interpretations and can be directly measured [8].

Assuming that the equivalent switching frequency is high enough and the capacitor voltages of all submodules are balanced at all times [10], [25], [26], according to the symmetry of MMC, taking the upper arm of phase a as an example, the small signal model of MMC power stage can be obtained by harmonic linearization [27]–[30]

$$\mathbf{Z}_l \hat{\mathbf{i}}_{au} = -\hat{\mathbf{v}}_p - \mathbf{M}_{au}\hat{\mathbf{u}}_{au} - \hat{\mathbf{m}}_{au}\mathbf{u}_{au} \quad (2)$$

$$\mathbf{Y}_c \hat{\mathbf{u}}_{au} = \mathbf{M}_{au}\hat{\mathbf{i}}_{au} + \mathbf{I}_{au}\hat{\mathbf{m}}_{au} \quad (3)$$

where $\hat{\mathbf{i}}_{au}$, $\hat{\mathbf{u}}_{au}$ and $\hat{\mathbf{m}}_{au}$ are small-signal vectors of upper arm current in phase a, sum of all submodule capacitor voltages in the phase a upper arm and modulation index of upper arm in phase a, $\hat{\mathbf{v}}_p$ is the vector of voltage small voltage perturbation in phase a, $\mathbf{Z}_l$ and $\mathbf{Y}_c$ are diagonal matrixes which represents the impedance of the arm inductor and the admittance of equivalent module capacitor. Corresponding to small signal variables, $\mathbf{I}_{au}$, $\mathbf{u}_{au}$ and $\mathbf{M}_{au}$ are Toeplitz matrixes of steady-state variables of upper arm current in phase a, sum of all submodule capacitor voltages in the phase a upper arm and modulation index of upper arm in phase a.

It is important to note that the given voltage perturbation will lead to a series of small-signal harmonic components at frequency $f_p \pm kf_1$, $k = 1, 2 \ldots n$, although infinite harmonics are generated in theory, harmonics at $f_p \pm kf_1$ will decline exponentially with the increase of k in fact. MMC model including 3rd harmonics of fundamental frequency f_1 is adequate for the dynamic analysis [31], [32], therefore, to balance the accuracy of model and the complexity of mathematical operation, harmonics up to $f_p \pm 3f_1$ are considered in all variables above in this article. Under positive-sequence and negative-sequence voltage perturbation in MMC AC side, the harmonics of small-signal components including arm currents, arm capacitor voltages, and arm modulation indexes have the relationships as Table 1 [9]. Only the differential-mode arm currents will flow to AC side of MMC.

TABLE 1. Relationships of small-signal harmonics.

Frequency	Sequence	Sign	Voltage perturbation in MMC AC side
f_p-3f_1	positive	CM	positive sequence
f_p-2f_1	negative	DM	
f_p-f_1	zero	CM	
f_p	positive	DM	
f_p+f_1	negative	CM	
f_p+2f_1	zero	DM	
f_p+3f_1	positive	CM	
f_p-3f_1	negative	CM	negative sequence
f_p-2f_1	zero	DM	
f_p-f_1	positive	CM	
f_p	negative	DM	
f_p+f_1	zero	CM	
f_p+2f_1	positive	DM	
f_p+3f_1	negative	CM	

CM represents common-mode, DM represents differential-mode.

III. MMC CONTROL STAGE SAMLL SIGNAL MODEL WITH TIME DELAY

Steady state variables of $\mathbf{M}_{au}$, $\mathbf{u}_{au}$ and $\mathbf{I}_{au}$ in (2) and (3) can be calculated from the output power of MMC [33]. Small signal vector of upper arm modulation index $\hat{\mathbf{m}}_{au}$ is related to the control system mode and parameters. In order to get the small signal impedance model, it is necessary to develop the small signal model of the control system.

A typical MMC cascade control is shown in Fig. 2, including power outer-loop control, phase current inner-loop control, circulating current control and phase-locked loop. Variable $i_j (j = a, b, c)$ represents phase current of MMC, and $i_{j-cir} (j = a, b, c)$ represents circulating current in each phase of MMC. All these loops have an influence on MMC control stage small signal model.

Because cascade control is utilized in MMC, the total time delay could be taken into account behind the modulation index as shown in Fig. 2 [16,34]. Influence of each control loop superimposes on the modulation index during the process of small signal modeling[35]. Thus the complex

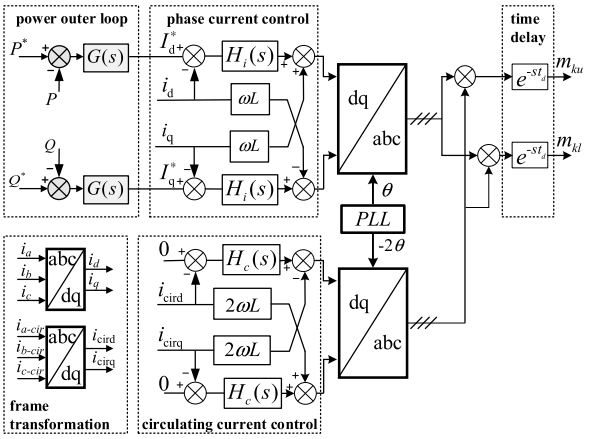

FIGURE 2. MMC control structure.

vector of arm modulation index can be expressed as:

$$\hat{\mathbf{m}}_{au} = (\mathbf{Q}_i + \mathbf{Q}_c + \mathbf{Q}_{\mathrm{P}\_i})\hat{\mathbf{i}}_{au} + (\mathbf{Q}_{\mathrm{P}\_u} + \mathbf{Q}_{\mathrm{PLL}})\hat{\mathbf{v}}_p \tag{4}$$

where $\mathbf{Q}_i$, $\mathbf{Q}_c$, $\mathbf{Q}_{\mathrm{P}\_i}$, $\mathbf{Q}_{\mathrm{P}\_u}$, $\mathbf{Q}_{\mathrm{PLL}}$ are the coefficient matrix of the phase current control loop, the circulating current control loop, the current effect component of power control loop, the voltage effect component of power control loop and PLL respectively. In this article, only the harmonics up to third fundamental frequency are considered, so these coefficient matrixes are all square matrixes of seven order, and the matrix coefficients are related to their control loop structure and controller parameters.

A. PHASE CURRENT CONTROL LOOP WITH DELAY

When a positive-sequence voltage perturbation is injected in MMC AC side, the coefficient matrix of the phase current control loop has been derived in [9] as:

$$\mathbf{Q}_i = diag[0\ a_1\ 0\ a_2\ 0\ 0\ 0] \tag{5}$$

where the frequencies corresponding to coefficients a_1 and a_2 are f_p–$2f_1$, and f_p respectively.

$$\begin{cases} a_1 = [H_i(j2\pi f_p) + j\omega L] \cdot T_{a1} \\ a_2 = [H_i(j2\pi(f_p - f_1)) - j\omega L] \cdot T_{a2} \end{cases} \tag{6}$$

where H_i is the phase current control transfer function.

But effect of time delay which are expressed as T_{a1} and T_{a2} in (6) are not considered in [9]. To overcome this drawback, the effect of time delay is derived as

$$\begin{cases} T_{a1} = e^{-j2\pi(f_p - 2f_1)t_\mathrm{d}} \\ T_{a2} = e^{-j2\pi f_p t_\mathrm{d}} \end{cases} \tag{7}$$

where t_d is the value of time delay.

B. CIRCULATING CURRENT CONTROL LOOP WITH TIME DELAY

When a positive-sequence voltage perturbation is injected in MMC AC side, the coefficient matrix of the circulating current control loop has been derived in [9] as:

$$\mathbf{Q}_c = diag[b_1\ 0\ 0\ 0\ b_2\ c\ b_3] \tag{8}$$

where the frequencies corresponding to coefficients b_1, b_2 and b_3 are f_p–$3f_1$, $f_p + f_1$, and f_p+$3f_1$ respectively.

$$\begin{cases} b_1 = [H_c(j2\pi(f_p - f_1)) + 2j\omega L] \cdot T_{b1} \\ b_2 = [H_c(j2\pi(f_p - f_1)) - 2j\omega L] \cdot T_{b2} \\ b_3 = [H_c(j2\pi(f_p + 5f_1)) + 2j\omega L] \cdot T_{b3} \end{cases} \tag{9}$$

where H_c is the circulating-current control transfer function.

However, the effect of time delay which are expressed as T_{b1}, T_{b2} and T_{b3} in (9) are not considered in [9], they are derived in this article as

$$\begin{cases} T_{b1} = e^{-j2\pi(f_p - 3f_1)t_\mathrm{d}} \\ T_{b3} = e^{-j2\pi(f_p + f_1)t_\mathrm{d}} \\ T_{b3} = e^{-j2\pi(f_p + 3f_1)t_\mathrm{d}} \end{cases} \tag{10}$$

where t_d is the value of time delay.

C. POWER OUTER LOOP CONTROL WITH DELAY

Active and reactive power of MMC can be expressed as:

$$\begin{cases} p = \dfrac{3}{2}\left(U_\mathrm{d} \cdot I_\mathrm{d} + U_\mathrm{q} \cdot I_\mathrm{q}\right) \\ q = \dfrac{3}{2}\left(U_\mathrm{q} \cdot I_\mathrm{d} - U_\mathrm{d} \cdot I_\mathrm{q}\right) \end{cases} \tag{11}$$

where U_d and U_q are d-axis and q-axis steady-state voltage of MMC, I_d and I_q are d-axis and q-axis steady-state current. So the small signal active and reactive power can be expressed as:

$$\begin{cases} \hat{p} = \dfrac{3}{2}\left[\left(U_\mathrm{d}\hat{i}_\mathrm{d} + U_\mathrm{q}\hat{i}_q\right) + \left(I_\mathrm{d}\hat{u}_\mathrm{d} + I_\mathrm{q}\hat{u}_\mathrm{q}\right)\right] \\ \hat{q} = \dfrac{3}{2}\left[\left(U_\mathrm{q}\hat{i}_\mathrm{d} - U_\mathrm{d}\hat{i}_\mathrm{q}\right) + \left(I_\mathrm{d}\hat{u}_\mathrm{q} - I_\mathrm{q}\hat{u}_\mathrm{d}\right)\right] \end{cases} \tag{12}$$

The small signal power includes effects of the small signal current and the small signal voltage as shown in (12).

First of all, the model of small signal current $\hat{i}_\mathrm{d}$ and $\hat{i}_q$ included in $U_\mathrm{d}\hat{i}_\mathrm{d} - U_\mathrm{q}\hat{i}$ and $U_\mathrm{q}\hat{i}_\mathrm{d} - U_\mathrm{d}\hat{i}_\mathrm{q}$ in (12) is established as below.

When a positive-sequence voltage perturbation is injected in MMC AC side, the effect to modulation index of DM current harmonics only whose frequencies are f_p and f_p–$2f_1$ should be analyzed [9]. Assuming the DM positive-sequence small signal current harmonic of frequency f_p is:

$$\begin{cases} \hat{i}_a = I_p \cos(2\pi f_p t) \\ \hat{i}_b = I_p \cos(2\pi f_p t - \dfrac{2}{3}\pi) \\ \hat{i}_c = I_p \cos(2\pi f_p t + \dfrac{2}{3}\pi) \end{cases} \tag{13}$$

According to the MMC cascade control as shown in Fig. 2, this small signal current harmonic is calculated to small signal active and reactive power in (12) after dq transformation, then these small signal harmonics flow into outer-loop controller $G(s)$ and inner-loop controller $H_i(s)$, finally modulation index is obtained after inverse dq transformation

and flowing through time delay. This whole process can be expressed as

$$\begin{aligned}\begin{bmatrix}\hat{m}_{a1}\\ \hat{m}_{b1}\\ \hat{m}_{c1}\end{bmatrix} &= \mathbf{T}_{\mathrm{dq}}^{\mathrm{T}}\begin{bmatrix}\frac{3}{2}\left(U_{\mathrm{d}}\hat{i}_{\mathrm{d}}+U_{\mathrm{q}}\hat{i}_{\mathrm{q}}\right)\cdot G(s)\cdot H_i(s)\\ \frac{3}{2}\left(U_{\mathrm{q}}\hat{i}_{\mathrm{d}}-U_{\mathrm{d}}\hat{i}_{\mathrm{q}}\right)\cdot G(s)\cdot H_i(s)\end{bmatrix}\\ &= \begin{bmatrix}k_1I_p\cos\left(2\pi\left(f_p-2f_1\right)t\right)\\ k_1I_p\cos\left(2\pi\left(f_p-2f_1\right)t+\frac{2}{3}\pi\right)\\ k_1I_p\cos\left(2\pi\left(f_p-2f_1\right)t-\frac{2}{3}\pi\right)\end{bmatrix}\\ &\quad+\begin{bmatrix}k_2I_p\cos\left(2\pi\left(f_p-2f_1\right)t-\frac{\pi}{2}\right)\\ k_2I_p\cos\left(2\pi\left(f_p-2f_1\right)t-\frac{\pi}{2}+\frac{2}{3}\pi\right)\\ k_2I_p\cos\left(2\pi\left(f_p-2f_1\right)t-\frac{\pi}{2}-\frac{2}{3}\pi\right)\end{bmatrix}\end{aligned} \tag{14}$$

where $\mathbf{T}_{\mathrm{dq}}^{\mathrm{T}}$ is inverse dq transformation, and

$$\begin{cases}\left[\hat{i}_{\mathrm{d}},\hat{i}_{\mathrm{q}},\hat{i}_0\right]^T=\mathbf{T}_{\mathrm{dq}}\left[\hat{i}_a,\hat{i}_b,\hat{i}_c\right]^T\\ k_1=1.5U_dG\left(j2\pi(f_p-f_1)\right)\cdot H_i\left(j2\pi(f_p-f_1)\right)\\ k_2=1.5U_qG\left(j2\pi(f_p-f_1)\right)\cdot H_i\left(j2\pi(f_p-f_1)\right)\end{cases} \tag{15}$$

where $\mathbf{T}_{\mathrm{dq}}$ is dq transformation.

When comparing (14) with (13), it could be found that small signal current harmonic at frequency f_p generates two small signal harmonics of frequency f_p-2f_1 in modulation index. The gains of these two signals are k_1 and k_2 separately, and the second signal has $\pi/2$ phase delay compared with the original small signal current harmonic which expressed as (13). So the coefficient matrix of the small signal phase current at frequency f_p to modulation index in power control loop can be expressed as:

$$\mathbf{Q}_{\mathrm{P}\_i1}=\begin{bmatrix}0&0&0&0&0&0&0\\ 0&0&0&d_1&0&0&0\\ &&&\mathbf{0}_{5\times7}&&&\end{bmatrix} \tag{16}$$

where

$$\begin{aligned}d_1=&\left(1.5U_d+1.5U_q\cdot e^{j(-\frac{\pi}{2})}\right)\cdot G\left(j2\pi(f_p-f_1)\right)\\ &\cdot H_i\left(j2\pi(f_p-f_1)\right)e^{-j2\pi(f_p-2f_1)t_{\mathrm{d}}}.\end{aligned} \tag{17}$$

Similarly, the coefficient matrix of the DM negative-sequence small signal phase current at frequency f_p-2f_1 to modulation index in power control loop can be expressed as:

$$\mathbf{Q}_{\mathrm{P}\_i2}=\begin{bmatrix}&&\mathbf{0}_{3\times7}&&&&\\ 0&d_2&0&0&0&0&0\\ &&\mathbf{0}_{3\times7}&&&&\end{bmatrix} \tag{18}$$

where

$$\begin{aligned}d_2=&\left(1.5U_d+1.5U_q\cdot e^{j(-\frac{\pi}{2})}\right)\cdot G\left(j2\pi(f_p-2f_1+f_1)\right)\\ &\cdot H_i\left(j2\pi(f_p-2f_1+f_{11})\right)e^{-j2\pi f_pt_{\mathrm{d}}}.\end{aligned} \tag{19}$$

So the coefficient matrix of the small signal phase current to modulation index in power control loop can be obtained as:

$$\mathbf{Q}_{\mathrm{P}\_i}=\mathbf{Q}_{\mathrm{P}\_i1}+\mathbf{Q}_{\mathrm{P}\_i2}. \tag{20}$$

Then the model of small signal voltage $\hat{u}_{\mathrm{d}}$ and $\hat{u}_{\mathrm{q}}$ included in $I_{\mathrm{d}}\hat{u}_{\mathrm{d}}+I_{\mathrm{q}}\hat{u}_{\mathrm{q}}$ and $I_{\mathrm{d}}\hat{u}_{\mathrm{q}}-I_{\mathrm{q}}\hat{u}_{\mathrm{d}}$ in (12) is established. Similar to the above analysis process, the coefficient matrix of the small signal voltage to modulation index in power control loop can be expressed as:

$$\mathbf{Q}_{\mathrm{P}\_u}=diag\left[\,0\;0\;0\;d_3\;0\;0\;0\,\right] \tag{21}$$

where

$$\begin{aligned}d_3=&\left(1.5I_{\mathrm{d}}+1.5I_{\mathrm{q}}\cdot e^{j(-\frac{\pi}{2})}\right)\cdot G\left(j2\pi(f_p-f_1)\right)\\ &\cdot H_i\left(j2\pi(f_p-f_1)\right)e^{-j2\pi f_pt_{\mathrm{d}}}.\end{aligned} \tag{22}$$

where t_{d} is the value of time delay.

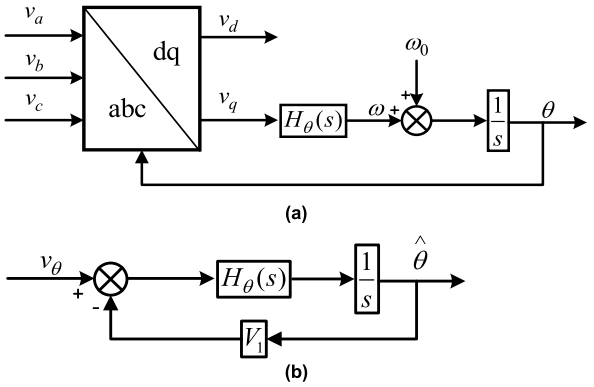

FIGURE 3. (a) Block diagram of a basic PLL and (b) its linearized model.

D. PHSE-LOCKED LOOP WITH DELAY

Block diagram of PLL and its small signal model is shown in Fig. 3. Contribution of PLL dynamics to the inner decoupled current control has been analyzed in [9], but the contribution of PLL dynamics to the outer control loop has not been discussed.

When MMC AC side is injected by a positive-sequence voltage perturbation with amplitude $\hat{V}_p$ and frequency f_p, the PLL output small signal phase is

$$\hat{\theta}=-j\frac{\hat{V}_p}{2}e^{j\varphi_p}\cdot G_\theta[j2\pi(f_p-f_1)] \tag{23}$$

where ϕ_p is phase angle of voltage perturbation, $G_\theta(s)$ is the closed-loop transfer function of PLL, and the frequency of $\hat{\theta}$ is f_p–f_1 [9].

So the dq transformation and inverse dq transformation will be affected by this PLL dynamic $\hat{\theta}$ accordingly:

$$\mathbf{T}_{\mathrm{dq}}(2\pi f_1t+\hat{\theta})=\underbrace{\mathbf{T}_{\mathrm{dq}}(2\pi f_1t)}_{\text{term A1}}+\underbrace{\hat{\theta}\cdot\mathbf{T}_{\mathrm{dq}}(2\pi f_1t+\frac{\pi}{2})}_{\text{term A2}} \tag{24}$$

$$\mathbf{T}_{\mathrm{dq}}^{\mathrm{T}}(2\pi f_1t+\hat{\theta})=\underbrace{\mathbf{T}_{\mathrm{dq}}^{\mathrm{T}}(2\pi f_1t)}_{\text{term B1}}+\underbrace{\hat{\theta}\cdot\mathbf{T}_{\mathrm{dq}}^{\mathrm{T}}(2\pi f_1t+\frac{\pi}{2})}_{\text{term B2}} \tag{25}$$

where term A2 and term B2 in (24) and (25) shows the effects of PLL dynamics compared with traditional dq transformation and inverse dq transformation [9].

Phase current and voltage contain a steady state (fundamental) and a series of small signal harmonics. Each dq-frame controller output also contains a steady state (DC) and a series of small signal harmonics. The small signal responses due to multiplication of term A1 with small signal harmonics in the phase currents and voltages, and small signal responses due to multiplication of term B1 with small signal harmonics in dq-frame controller outputs have been captured in Section III-A, III-B and III-C. However, multiplication of term A2 with steady state (fundamental) components in the phase currents and voltages, and multiplication of term B2 with steady state (DC) components in dq-frame controller outputs will also generate small signal responses because of PLL dynamics. So these small signal responses caused by term A2 and B2 should be analyzed: the steady state (DC) components in dq-frame controller outputs will generate small signal harmonics at frequency f_p-2f_1 and f_p after operation by term B2 in (25); the steady state (fundamental) components in the phase currents and voltages will generate two small signal harmonic at frequency f_p-2f_1 and f_p after operation by term A2 in (24).

The specific analysis is as follows.

Assuming steady state value of modulation index are M_d, M_q in dq-frame and M_1 for phase a in abc-frame respectively. M_d and M_q will generate a fundamental component after transformation by $\mathbf{T}_{\mathrm{dq}}^{\mathrm{T}}(2\pi f_1 t+\frac{\pi}{2})$ in (25), and then create a component at frequency f_p-2f_1 and f_p by angle perturbation $\hat{\theta}$ of term B2 in (25). The small signal component at frequency f_p is

$$0.5\mathbf{M}_1 G_\theta[j2\pi(f_p-f_1)]\cdot\hat{V}_p e^{j\varphi_p}, \tag{26}$$

and the small signal component at frequency f_p-2f_1 is

$$-0.5\mathbf{M}_1^* G_\theta[j2\pi(f_p-f_1)]\cdot\hat{V}_p e^{j\varphi_p} \tag{27}$$

where, "$*$" denotes complex conjugation.

Taking the current inner-loop as an example, the steady state (fundamental) components in the phase currents which is denoted as $\mathbf{I}_1$ for phase a will generate components at frequency f_p-f_1 after operation by term A2 in (24), then these components will flow through current inner-loop controller $H_i(s)$, small signal components at frequency f_p-2f_1 and f_p are created after operation by term B1 in (25) at last. The small signal component at frequency f_p is

$$-0.5\mathbf{I}_1 G_\theta[j2\pi(f_p-f_1)]\cdot H_i[(j2\pi(f_p-f_1)-jK_{id}]\cdot\hat{V}_p e^{j\varphi_p} \tag{28}$$

and the small signal component at frequency f_p-2f_1 is

$$0.5\mathbf{I}_1^* G_\theta[j2\pi(f_p-f_1)]\cdot H_i[(j2\pi(f_p-f_1)-jK_{id}]\cdot\hat{V}_p e^{j\varphi_p}. \tag{29}$$

For power outer-loop control, the steady state (fundamental) components in the phase currents and voltages which is denoted as $\mathbf{I}_1$ and $\mathbf{U}_1$ for phase a will also generate small signal components at frequency f_p-2f_1 and f_p which are similar to the analysis of the current inner-loop. It should be noted that the power outer-loop controller $G(s)$ needs to be considered. In addition, the response of the phase angle perturbation to circulating current control loop can be neglected because the circulating current in the arm has been suppressed small enough.

Based on the analysis above, the contribution of PLL dynamics to modulation index under a positive-sequence voltage perturbation can be expressed by $\mathbf{Q}_{\mathrm{PLL}}\hat{\mathbf{v}}_p$, where $\mathbf{Q}_{\mathrm{PLL}}$ is

$$\mathbf{Q}_{\mathrm{PLL}}=\begin{bmatrix}0&0&0&0&0&0&0\\0&0&0&g_2&0&0&0\\0&0&0&0&0&0&0\\0&0&0&g_1&0&0&0\\&&&\mathbf{0}_{3\times7}&&&\end{bmatrix} \tag{30}$$

where

$$\begin{aligned}g_1=&[0.5\mathbf{M}_1 G_\theta(j2\pi(f_p-f_1))\\&-0.5\mathbf{I}_1 G_\theta(j2\pi(f_p-f_1))\cdot H_i((j2\pi(f_p-f_1)-jK_{id})\\&+0.5\mathbf{I}_1 G_\theta(j2\pi(f_p-f_1))\cdot G(j2\pi(f_p-f_1))\\&\cdot H_i((j2\pi(f_p-f_1)-jK_{id})\\&-0.5\mathbf{U}_1^* G_\theta(j2\pi(f_p-f_1))\cdot G(j2\pi(f_p-f_1))\\&\cdot H_d((j2\pi(f_p-f_1))]\hat{V}_p\cdot T_{g1}\end{aligned} \tag{31}$$

$$\begin{aligned}g_2=&[-0.5\mathbf{M}_1^* G_\theta(j2\pi(f_p-f_1))\\&+0.5\mathbf{I}_1^* G_\theta(j2\pi(f_p-f_1))\cdot H_i((j2\pi(f_p-f_1)-jK_{id})\\&-0.5\mathbf{I}_1^* G_\theta(j2\pi(f_p-f_1))\cdot G(j2\pi(f_p-f_1))\\&\cdot H_i((j2\pi(f_p-f_1)-jK_{id})\\&+0.5\mathbf{U} G_\theta(j2\pi(f_p-f_1))\cdot G(j2\pi(f_p-f_1))\\&\cdot H_d((j2\pi(f_p-f_1))]\hat{V}_p\cdot T_{g2}\end{aligned} \tag{32}$$

where

$$\begin{cases}T_{g1}=e^{j\varphi_p}e^{-j2\pi f_p t_{\mathrm{d}}}\\T_{g2}=e^{-j2\pi(f_p-2f_1)t_{\mathrm{d}}}\end{cases}$$

accounts for the effect of time delay, t_{d} is the value of time delay.

All the coefficient matrixes of control system are derived under a positive-sequence voltage perturbation, the coefficient matrixes of control system derived under a negative-sequence voltage perturbation have a similar derivation process, which will not be repeated here.

In summary, the control small signal model including power outer-loop control, phase current inner-loop control, circulating current control and PLL dynamics is

$$\hat{\mathbf{m}}_{au}=(\mathbf{Q}_i+\mathbf{Q}_c+\mathbf{Q}_{\mathrm{P\_}i})\hat{\mathbf{i}}_{au}+(\mathbf{Q}_{\mathrm{P\_}u}+\mathbf{Q}_{\mathrm{PLL}})\hat{\mathbf{v}}_p \tag{33}$$

where $\mathbf{Q}_i$ is defined by (5), $\mathbf{Q}_c$ by (8), $\mathbf{Q}_{\mathrm{P\_}i}$ by (20), $\mathbf{Q}_{\mathrm{P\_}u}$ by (21), and $\mathbf{Q}_{\mathrm{PLL}}$ by (30).

IV. VALIDATION AND ANALYSIS OF MMC SEQUENCE IMPEDANCE MODEL

The sequence impedance model is derived considering phase current control loop, circulating current control loop, power outer loop control, PLL and time delay, the model is verified by simulation. Then the influences of key parameters on impedance models are discussed, which include parameters of phase current controllers, power outer loop control, and time delay.

A. VERIFICATION OF IMPEDANCE MODEL

A single matrix equation can be obtained by substituting the power stage small signal model (2) into (3) to eliminate $\hat{\mathbf{u}}_{au}$:

$$(\mathbf{U}+\mathbf{Z}_l^{-1}\mathbf{M}_{au}\mathbf{Y}_c^{-1}\mathbf{M}_{au})\hat{\mathbf{i}}_{au}+\mathbf{Z}_l^{-1}\hat{\mathbf{v}}_p +\mathbf{Z}_l^{-1}(\mathbf{u}_{au}+\mathbf{M}_{au}\mathbf{Y}_c^{-1}\mathbf{I}_{au})\hat{\mathbf{m}}_{au}=\mathbf{0} \quad (34)$$

where $\mathbf{U}$ is a 7×7 unity matrix.

Relationship of small signal $\hat{\mathbf{v}}_p$ and $\hat{\mathbf{i}}_{au}$ can be obtained by substituting (33) into (34)

$$\left[\begin{array}{l}\mathbf{U}+\mathbf{Z}_l^{-1}\mathbf{M}_{au}\mathbf{Y}_c^{-1}\mathbf{M}_{au}+\\ \mathbf{Z}_l^{-1}(\mathbf{u}_{au}+\mathbf{M}_{au}\mathbf{Y}_c^{-1}\mathbf{I}_{au})\cdot(\mathbf{Q}_i+\mathbf{Q}_c+\mathbf{Q}_{\mathrm{P}\_i})\end{array}\right]\hat{\mathbf{i}}_{au} +\mathbf{Z}_l^{-1}\left[\mathbf{U}+(\mathbf{u}_{au}+\mathbf{M}_{au}\mathbf{Y}_c^{-1}\mathbf{I}_{au})(\mathbf{Q}_{\mathrm{P}\_u}+\mathbf{Q}_{\mathrm{PLL}})\right]\hat{\mathbf{v}}_p=\mathbf{0} \quad (35)$$

Based on this, a 7×7 admittance matrix of small signal upper arm current $\hat{\mathbf{i}}_{au}$ to a perturbation $\hat{\mathbf{v}}_p$ in AC terminal voltage can be modeled as

$$\mathbf{Y}=\left[\begin{array}{l}\mathbf{U}+\mathbf{Z}_l^{-1}\mathbf{M}_{au}\mathbf{Y}_c^{-1}\mathbf{M}_{au}+\\ \mathbf{Z}_l^{-1}(\mathbf{u}_{au}+\mathbf{M}_{au}\mathbf{Y}_c^{-1}\mathbf{I}_{au})\cdot(\mathbf{Q}_i+\mathbf{Q}_c+\mathbf{Q}_{\mathrm{P}\_i})\end{array}\right]^{-1} \cdot\mathbf{Z}_l^{-1}\left[\mathbf{U}+(\mathbf{u}_{au}+\mathbf{M}_{au}\mathbf{Y}_c^{-1}\mathbf{I}_{au})(\mathbf{Q}_{\mathrm{P}\_u}+\mathbf{Q}_{\mathrm{PLL}})\right] \quad (36)$$

Since the phase current is twice the arm current, the input impedance of MMC at frequency f_p is

$$Z(f_p)=\frac{1}{2Y(4,4)} \quad (37)$$

where $Y(4,4)$ is the (4,4)th element of $\mathbf{Y}$.

To verify the analytical models above, simulation models based on sweeping frequency method are established in MATLAB/Simulink, and parameters in simulation models are listed in Table 2. The bode plot of MMC impedance and simulation results are depicted in Fig. 4. The analytical models match well with the simulation results which proves the accuracy of the model proposed in this article. As shown in Fig.4, the positive-sequence model and negative-sequence model are almost the same at higher frequency but are very different at low frequency. And it should be noted that the phase of impedance becomes over 90° as the frequency increases above 800Hz, which brings a negative damping.

B. INFLUENCE OF TIME DELAY

Different from existing literatures, time delay is especially considered in this article. Taking positive sequence as an example, the influence of control loop and controller parameters on impedance is analyzed.

Fig. 5 shows the influence of time delay. As shown in Fig.5(a), the impedance is significantly different at middle and high frequency when considering delay or not. The impedance changes obviously with the increase of time delay.

In order to show the difference better, Fig. 5(b) shows the zoomed-in results. As the delay increases, the magnitude and phase of impedance increase a lot at high frequency. It should be noted that there is a huge difference in phase angle between impedance with and without delay. According to Fig. 5(b), the phase angle of impedance without delay is always less than 90°, however, the phase angle of impedance with time delay exceeds 90° at a high frequency point. So the time delay will bring a negative damping to the impedance at high frequency, which may cause the MMC to oscillate with the power grid system. And the greater the delay, the lower the frequency point at which the impedance phase exceeds 90°.

TABLE 2. Parameters of MMC-HVDC.

Symbol	Description	Value
U_{dc}	rated DC voltage	500kV
P	rated power	750MW
V_{g}	rated AC voltage	260kV
C_m	submodule capacitance	7mF
N	number of submodules/arm	244
L	arm inductance	100mH
r_L	arm resistance	0.3Ω
L_{g}	grid inductance	55mH
C_{g}	grid capacitance	1.4μF
R_g	grid resistance	20Ω
$kp+ki/s$	PI controller of current loop	0.6+8/
$kp_{uter}+ki_{uter}/s$	PI controller of power loop	0.0002+100/s
$kp_{cir}+ki_{cir}/s$	PI controller of circulating current loop	150+1000/s
$kp_{pll}+ki_{pll}/s$	PI controller of PLL	200+2000/s
t_{d}	time delay	300μs

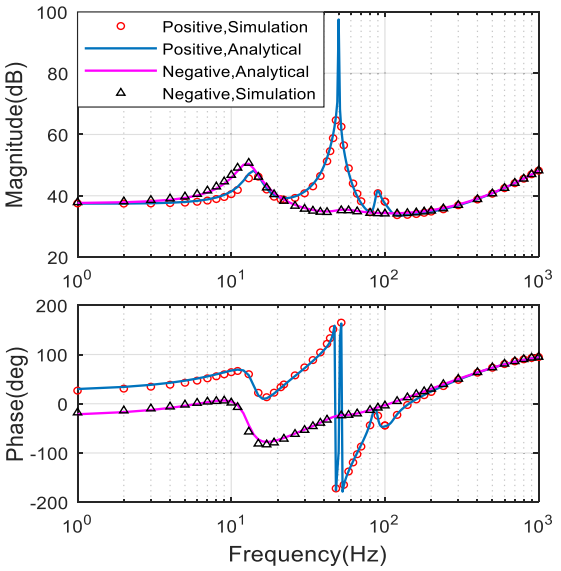

FIGURE 4. Analytical and simulation results of MMC impedance.

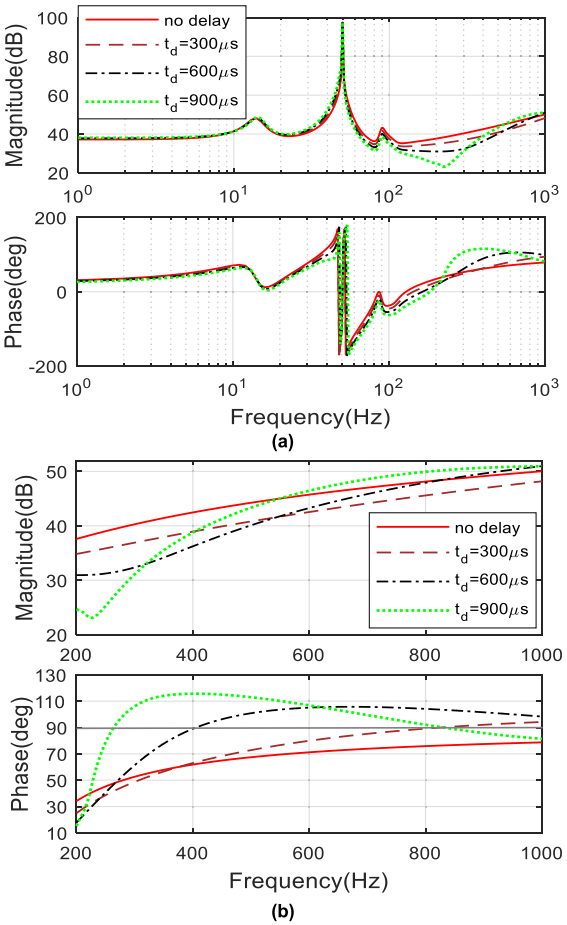

FIGURE 5. Impedance with changing digital delay. (a)Full scale, (b)Zoomed-in Figure.

This means that as the time delay increases, the frequency at which the impedance showing negative damping shifts to lower frequency.

The negative damping caused by the delay will affect the stability of the system, especially the high-frequency stability, so the digital delay cannot be ignored during the modeling process, and should be given full attention.

C. ANALYSIS OF CONTROLLER PARAMETERS

Firstly, the influence of parameters of current loop controller without and with time delay are shown in Fig. 6 and Fig. 7 separately.

Three sets of current controller *kp* (i.e., 0.2, 0.6 and 1.2) are chosen. If time delay is not considered, the influence of parameters of current loop controller is shown in Fig. 6. As shown in Fig. 6, the current loop controller proportional coefficient *kp* has great influence on the MMC impedance. As the *kp* increases, the magnitude increases a lot, while the phase increases below 50Hz and decreases above 50Hz. It should be noted that, for all of this cases, the phase is limited to the 90° range.

Under the same *kp* conditions, if delay is considered and fixed at 300μs, then the impedance is re-depicted in Fig. 7(a).

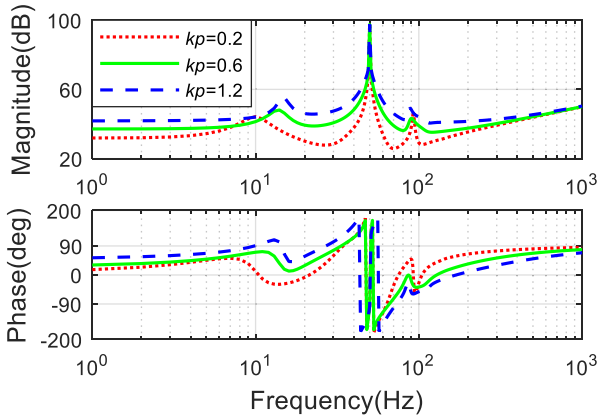

FIGURE 6. Impedance of MMC when current loop controller $kp = 0.2$, 0.6, and 1.2 without time delay.

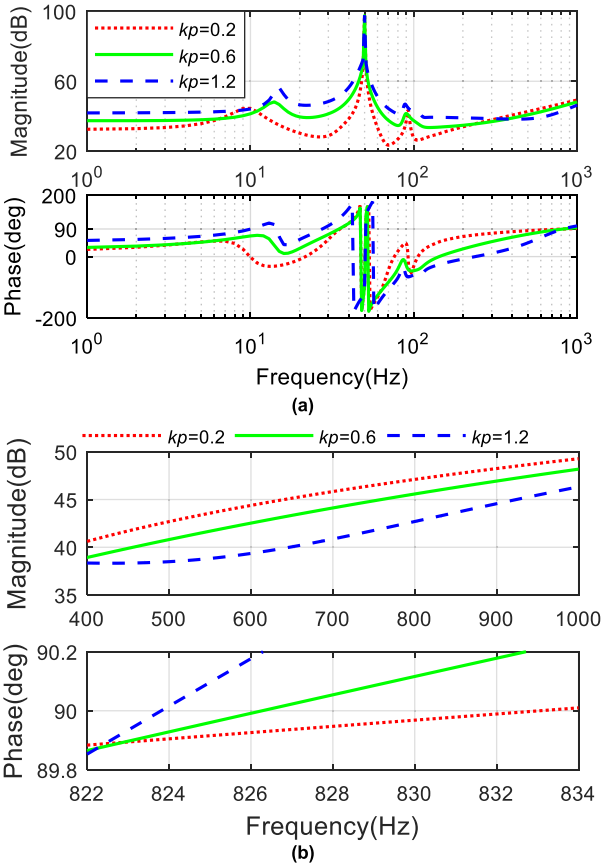

FIGURE 7. Impedance of MMC when current loop controller $kp = 0.2$, 0.6, and 1.2 with time delay $t_d = 300\mu$s. (a) Full scale. (b) Zoom-in figure.

As the *kp* increases, the magnitude becomes larger, while the phase rises more smoothly. Compared with Fig. 6, it could be seen that the impedance characteristics have a big difference at high frequency above 800Hz. To see it more clearly, the zoom-in figurer is shown in Fig. 7(b), for the three cases, the phase exceeds 90° at high frequency. Meanwhile, as the *kp* increases, the magnitude becomes higher, and the frequency point at which the phase exceeds 90° shifts to a lower frequency point.

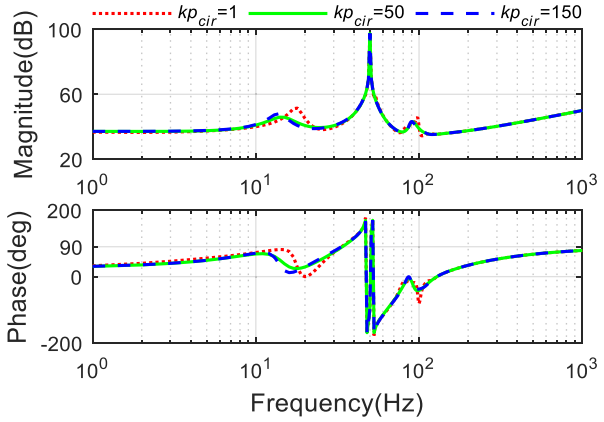

FIGURE 8. Impedance of MMC when circulating current loop controller kp_{cir} = 1, 50, and 150 without time delay.

Secondly, three sets of circulating current controller kp_{cir} (i.e., 1, 50 and 150) are chosen. If time delay is not considered, the influence of parameters of circulating current loop controller is shown in Fig. 8. As shown in Fig. 8, the circulating current loop controller proportional coefficient kp_{cir} seems to affect only two resonance peaks around 15Hz and 100Hz. It should be noted that, for all of this cases, the phase is limited to the 90° range.

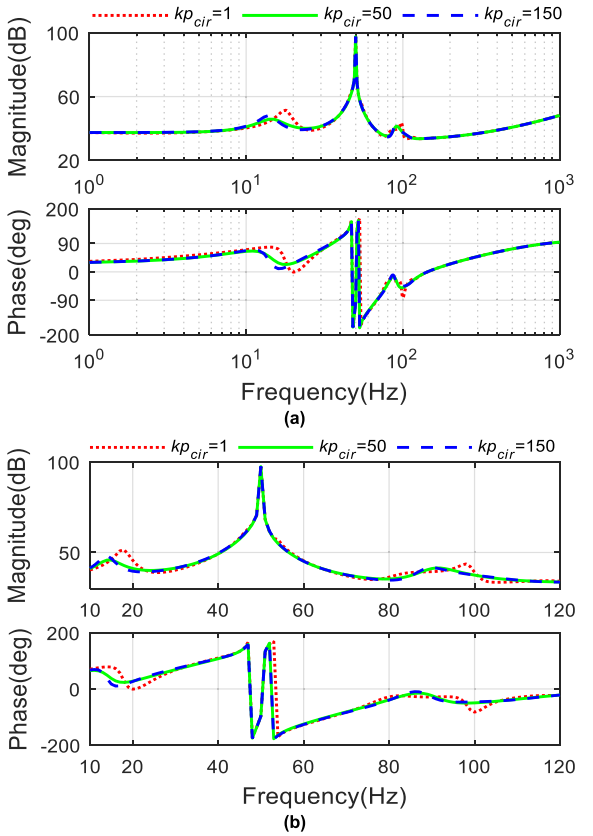

FIGURE 9. Impedance of MMC when circulating current loop controller kp_{cir} = 1, 50, and 150 with time delay $t_d = 300\mu$s. (a) Full scale. (b) Zoom-in figure.

Under the same kp_{cir} conditions, if delay is considered and fixed at 300μs, then the impedance is re-depicted in Fig. 9 (a).

Compared with Fig. 8, it could be seen that the impedance characteristics are almost the same with which shown in Fig.8 at low and middle frequency, but the phases are different at high frequency. As shown in Fig. 9(a), the circulating current loop controller proportional coefficient kp_{cir} seems to affect only two resonance peaks around 15Hz and 100Hz. To see it more clearly, the zoom-in figurer is shown in Fig. 9(b), as proportional coefficient kp_{cir} increases, the resonance peaks around 15Hz and 100Hz shift to lower frequency, while the magnitude and phase of resonance peaks both decrease. Because parameters of circulating current loop controller affect the ability of suppressing the circulating current, if the kp_{cir} is not large enough to suppress the circulating current, magnitudes of the resonance peaks around 15Hz and 100Hz will be larger and phases will be smaller. In particular, when these parameters are not properly designed, the phase of the resonance peak around 100Hz might be smaller than −90°, which brings a negative damping effect, which may cause the MMC to oscillate with the power grid system.

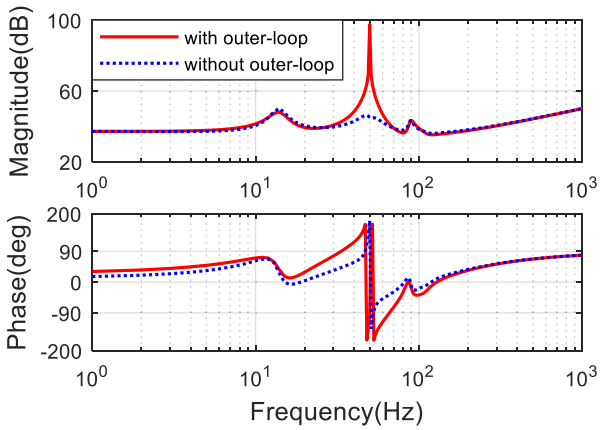

FIGURE 10. Impedance with/without power outer-loop control when delay is not considered.

Thirdly, if time delay is not considered, the impact of power outer loop control on impedance is shown in Fig. 10. It can be found that the impedance with outer loop changes a lot compared with the impedance without considering outer loop, so modeling with consideration of outer loop is very meaningful. It should be noted that, without considered time delay, the phase is limited to the 90° range. The outer loop cannot be ignored during the modeling process, and the modeling without considering the outer loop will affect the accuracy of the system stability analysis and even lead to erroneous analysis results.

Under the same conditions, if delay is considered and fixed at 300μs, then the impedance is re-depicted in Fig. 11. At low and middle frequency area, the impedance characteristics are almost the same compared with Fig. 10. However, the impedance phase exceeds 90° at high frequency when time delay is considered.

According to the above analysis, the influence of delay on impedance characteristics is summarized as follows.

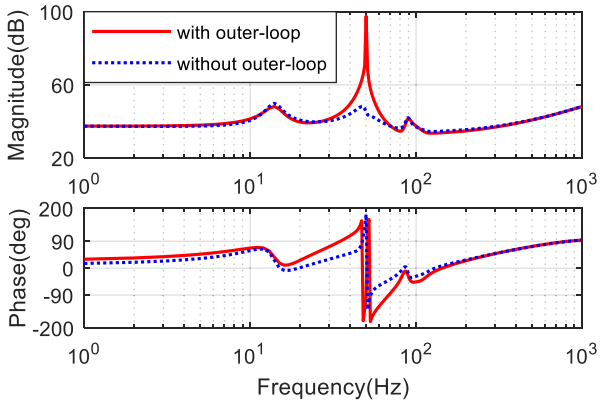

FIGURE 11. Impedance with/without power outer-loop control with time delay $t_d = 300\mu$s.

The phase angle of impedance with time delay exceeds 90° at a high frequency point. No matter how parameters of current loop, circulating current control loop and outer loop change, when time delay is considered, the phase angle of impedance with time delay will still exceed 90° at a relative high frequency, and the frequency point at which the phase exceeds 90° may shift. This means that a negative damping at high frequency is caused by time delay. This negative damping will affect the stability of the system, especially the high-frequency stability, so the time delay cannot be ignored during the modeling process, and should be given full attention. The oscillation caused by the delay will be analyzed in detail in the next section.

V. STABILITY ANALYSIS AND STABILIZATION CONTROL STATEGY

This section analyzes the stability of grid-connected MMC based on the impedance modeled above, and proposes a stabilization control strategy to improve its stability. The impedance model including stabilization control strategy is deduced, the parameters of stabilization control strategy are optimized based on this model. The effectiveness of impedance model and stabilization control strategy is verified by simulation.

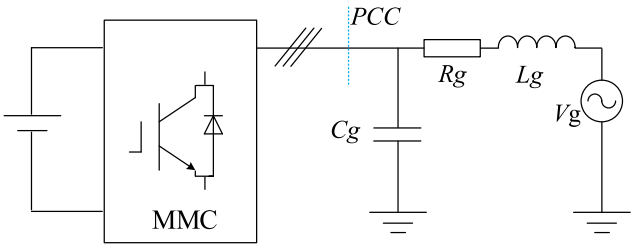

FIGURE 12. Schematic diagram of the grid-connected MMC system.

A. STABILITY ANALYSIS

In this work, a MMC operating in power outer-loop and current inner-loop control mode is studied. A grid-connected MMC system is defined in Fig. 12. Parameters of MMC and grid are presented in Table 2, and the impedance of transmission line and transformer are included as equivalent grid impedance, and grid impedance includes equivalent grid inductance L_g, equivalent grid resistance r_g and equivalent grid capacitance C_g. The MMC under power control mode can be regarded as a current source, and the topology of this grid-connected system can be simplified as Fig. 13.

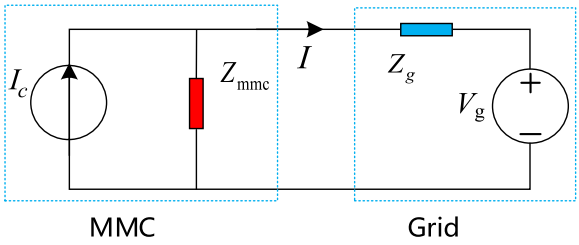

FIGURE 13. Simplified topology of MMC connecting to grid.

As shown in Fig. 13, the current flowing through grid can be expressed as:

$$I = \left(I_c - \frac{V_g}{Z_{mmc}}\right) \cdot \frac{1}{1 + Z_g/Z_{mmc}} \tag{38}$$

where the Z_{mmc} is the impedance of MMC, and the Z_g is the grid impedance.

According to Nyquist stability criterion [8], the stability of this system depends on the stability of impedance ratio Z_g/Z_{mmc} under the condition that MMC and grid are both stable independently. Now the stability of impedance ratio is analyzed as below.

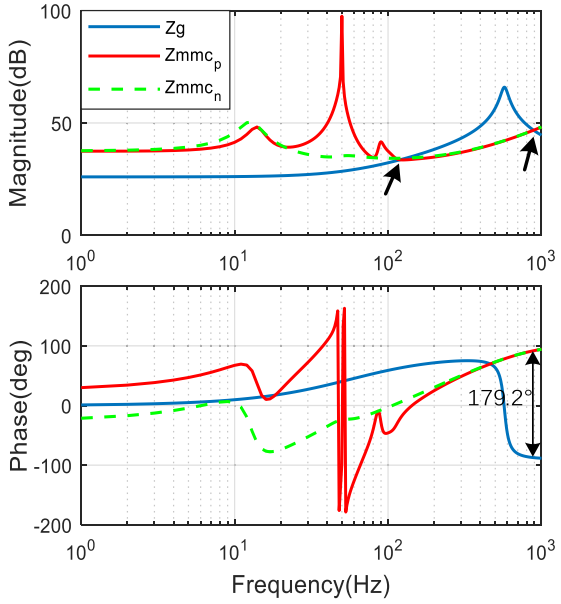

FIGURE 14. Impedance bode diagram MMC and grid with time delay $t_d = 300\mu$s.

When time delay is considered, the bode diagrams of Z_{mmc} and Z_g is depicted in Fig. 14, the red line and green

line represent the positive-sequence and negative-sequence impedance of MMC respectively, and the blue line represents impedance of grid. The grid impedance intersects with the MMC positive-sequence and negative-sequence impedance at two different frequencies including 116Hz and 888Hz. The phase difference at 116Hz between grid and MMC positive-sequence impedance is 90°, between grid and MMC negative-sequence impedance is 58.4°, indicating sufficient phase margin in system stability. However, the phase difference is 179.2° at 888Hz, which indicates the phase margin is too small and may cause harmonic resonance at this frequency.

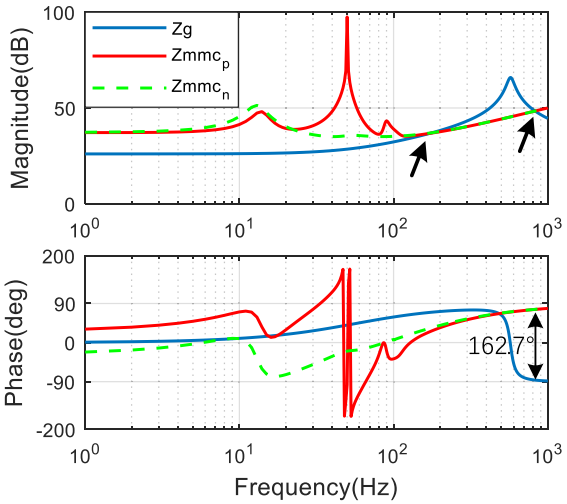

FIGURE 15. Impedance bode diagram of MMC and grid when time delay is not considered.

Compared with Fig. 14, the bode diagrams of Z_{mmc} and Z_g without time delay is depicted in Fig. 15. The grid impedance intersects with the MMC positive-sequence and negative-sequence impedance at 172Hz and 827Hz, whose phase differences are 94.5° and 162.7° respectively, indicating sufficient phase margin in system stability.

To verify the analysis above, the simulation results with and without time delay are shown in Fig. 16 and Fig. 17 separately. Fig. 16 shows that MMC output current and voltage waveforms oscillate violently when time delay is considered, which verified the stability margin of system is insufficient. And the harmonic spectrum of MMC output current in Fig. 18 shows that current oscillation arises at 888Hz, which agree well with the analysis based on impedance matching in Fig.14. However, when time delay is not considered, simulation results in Fig. 17 show that the HVDC system operates stably, agree well with the analysis based on impedance matching in Fig 15. The simulation results in Fig. 16 and Fig. 17 prove that the stability analysis above based on impedance is correct.

According to the stability analysis above based on impedance and simulation results, it is clearly shown that the time delay is the core cause to the system high-frequency oscillation. The time delay leads a negative damping to MMC

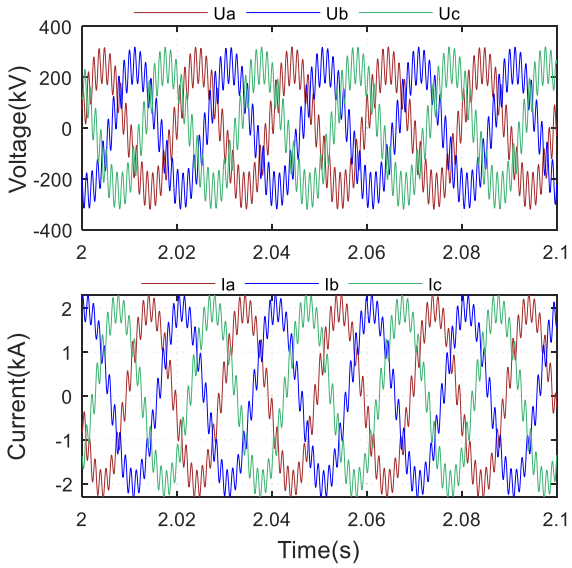

FIGURE 16. MMC terminal voltage and output current simulation with time delay considered.

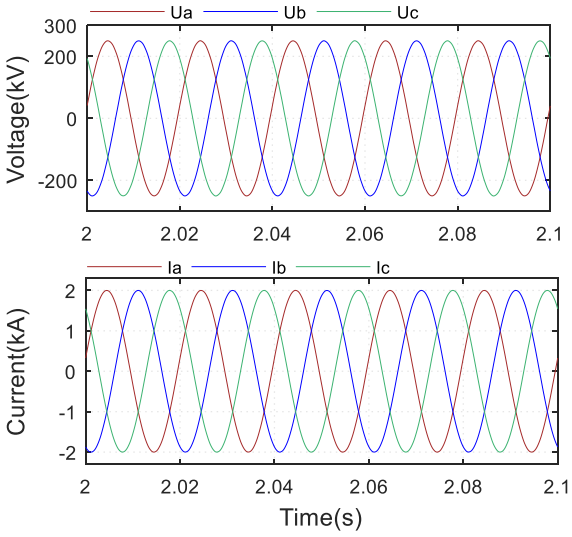

FIGURE 17. MMC terminal voltage and output current simulation without time delay.

impedance at high frequency, and this negative damping causes insufficient stability margin to the grid-connected MMC system. To cope with the system oscillation, a stabilization method is proposed in next section.

B. STABILIZATION CONTROL STRATEGY

1) STRUCTURE OF STABILIZATION CONTROL

Some papers point out that adding passive damping can suppress system oscillation, however, this method will increase system loss. So this article proposes a stabilization control strategy to suppress the oscillations. The detailed control strategy is depicted in the blue block diagram in Fig.19.

The PCC voltage $v_i(i = a, b, c)$ is sampled and passed through a quasi-proportional resonance (QPR) controller, and the negative of QPR output is added in the modulation index.

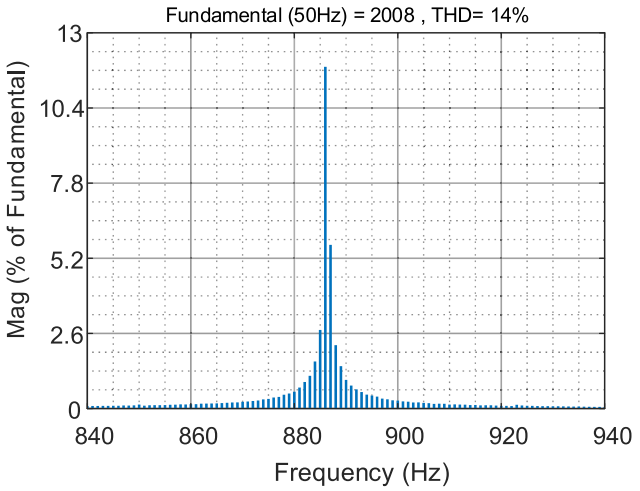

FIGURE 18. Harmonic spectrum of MMC output current.

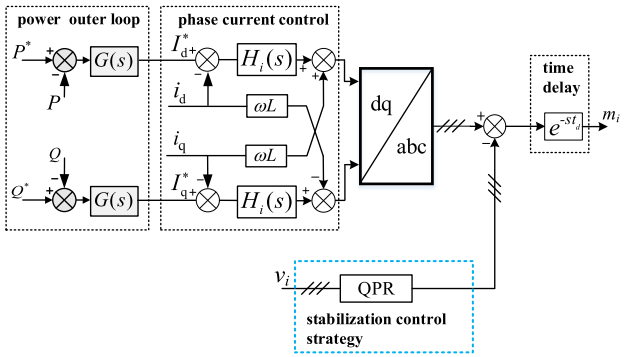

FIGURE 19. Block diagram of stabilization control strategy.

In this way, the voltages in opposite direction to the system oscillation are output from MMC terminal to mitigate the oscillation harmonics.

The transfer function of the QPR is defined as:

$$G_{\mathrm{QPR}}(s) = \frac{2k_r\omega_c s}{s^2 + 2\omega_c s + \omega_0} \tag{39}$$

where the value of QPR controller's resonance frequency ω_0 is the frequency of the system oscillation ($\omega_0 = 2\pi \times 888$). Adjusting the control parameters of QPR can change the MMC impedance, thus changing the phase margin at the impedance intersection to improve the system stability.

2) IMPEDANCE MODEL INCLUDING STABILIZATION CONTROL STRATEGY

Obviously, stabilization control strategy will change MMC impedance characteristics. However, most papers haven't discussed the impedance modeling including their proposed additional stabilization control strategy. In this article, the impedance including proposed stabilization control strategy is deduced as below.

Similar to the modeling process of impedance shown in section III, the voltage perturbation in MMC AC side flows through the QPR controller and generates a corresponding effect on the modulation index. This effect can be expressed as:

$$\hat{\mathbf{m}}_s = \mathbf{Q}_s \hat{\mathbf{v}}_p \tag{40}$$

where

$$\mathbf{Q}_s = diag[0\ 0\ 0\ g_3\ 0\ 0\ 0] \tag{41}$$

Based on the above analysis and the sequence relationships presented in Table 1, the parameter of coefficient matrix $\mathbf{Q}_s$ can be expressed as:

$$g_3 = -\frac{2k_r\omega_c(j2\pi f_p)}{(j2\pi f_p)^2 + 2\omega_c(j2\pi f_p) + \omega_0} e^{-j2\pi f_p t_d}. \tag{42}$$

Thus the small signal modulation index in (33) should be revised to

$$\hat{\mathbf{m}}'_{au} = \left(\mathbf{Q}_i + \mathbf{Q}_c + \mathbf{Q}_{\mathrm{P\_}i}\right)\hat{\mathbf{i}}_{au} + \left(\mathbf{Q}_{\mathrm{P\_}u} + \mathbf{Q}_{\mathrm{PLL}} + \mathbf{Q}_s\right)\hat{\mathbf{v}}_p \tag{43}$$

where $\mathbf{Q}_s$ is added to the modulation index.

Similarly, (36) should also be revised to

$$\mathbf{Y}' = \begin{bmatrix} \mathbf{U} + \mathbf{Z}_l^{-1}\mathbf{M}_{au}\mathbf{Y}_c^{-1}\mathbf{M}_{au} + \\ \mathbf{Z}_l^{-1}\left(\mathbf{u}_{au} + \mathbf{M}_{au}\mathbf{Y}_c^{-1}\mathbf{I}_{au}\right)\cdot\left(\mathbf{Q}_i + \mathbf{Q}_c + \mathbf{Q}_{\mathrm{P\_}}\right) \end{bmatrix}^{-1} \cdot\mathbf{Z}_l^{-1}\left[\mathbf{U} + \left(\mathbf{u}_{au} + \mathbf{M}_{au}\mathbf{Y}_c^{-1}\mathbf{I}_{au}\right)\left(\mathbf{Q}_{\mathrm{P\_}u} + \mathbf{Q}_{\mathrm{PLL}} + \mathbf{Q}_s\right)\right] \tag{44}$$

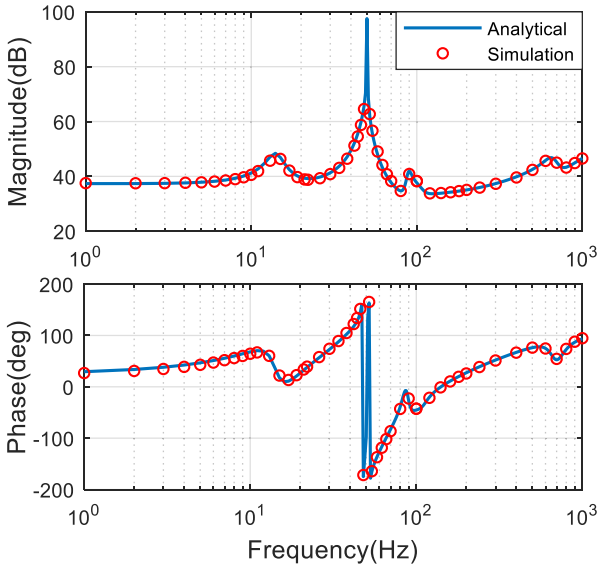

FIGURE 20. Analytical and simulation results of impedance including stabilization control strategy.

Then the impedance including additional stabilization control strategy is obtained as:

$$Z'(f_p) = \frac{1}{2Y'(4,4)} \tag{45}$$

Taking positive sequence impedance as an example, the bode plot of impedance including additional stabilization control strategy and simulation results are depicted in Fig. 20.

The analytical models match well with the simulation results which proves the accuracy of the analytical model proposed above. Based on this accurate impedance model considering the stabilization control strategy, parameters of the stabilization control strategy could be designed conveniently.

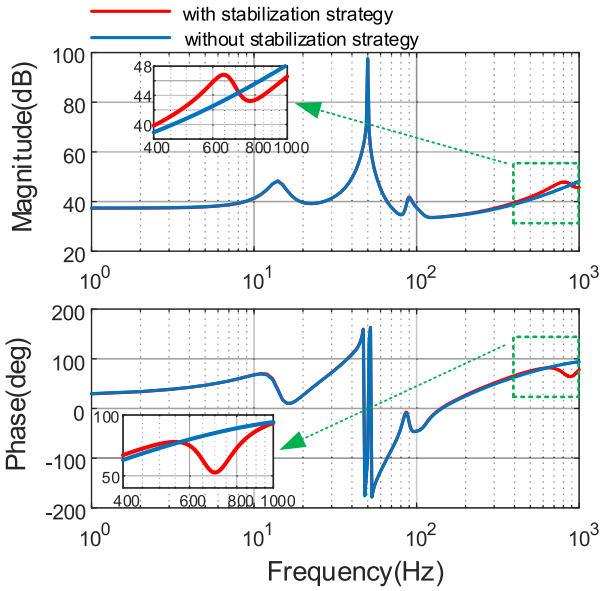

FIGURE 21. Comparison of impedance with/without stabilization control strategy.

3) PARAMETERS OPTIMIZATION OF STABILIZATION CONTROL

Fig. 21 shows the comparison of impedance which includes the stabilization control strategy or not. The low-frequency and middle-frequency characteristics of impedance with and without stabilization control strategy are almost the same. But the high-frequency impedance characteristics around resonance frequency are quite different compared with the impedance excluding stability strategy, especially the phase angle decreases to below 90°, which avoids negative damping.

The intersection of this MMC impedance with stabilization control strategy and grid impedance will change with the varying of QPR parameters. In order to improve the stability margin of the system as much as possible, the parameters of QPR controller in stabilization control strategy should be optimized.

Firstly, the parameter ω_c of QPR controller remains unchanged ($\omega_c = 2\pi \times 200$), and then the influence of the value of k_r on the phase margin of impedance intersection is studied.

The phase margin at impedance intersection of MMC and grid changes with the changing k_r which is depicted clearly in Fig.22. And the phase margin becomes the maximum value when k_r is equal to 0.22.

Then, the parameter k_r of QPR controller remain unchanged ($k_r = 0.22$), and the influence of the value of

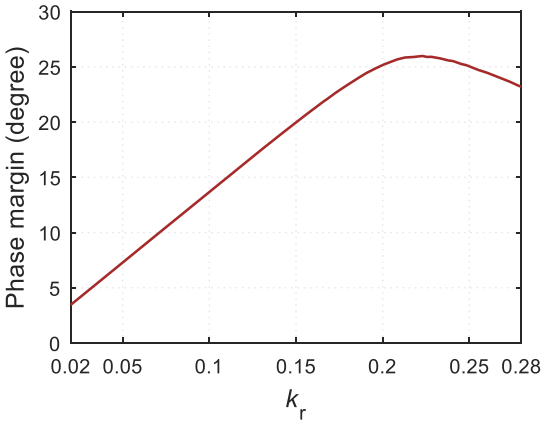

FIGURE 22. Phase margin as k_r changes.

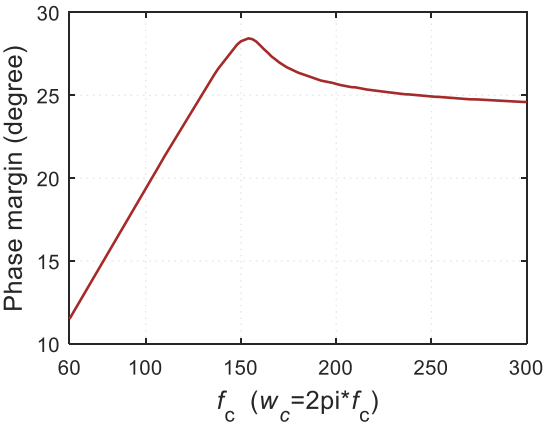

FIGURE 23. Phase margin as f_c changes.

$f_c(\omega_c = 2\pi \times f_c)$ on the phase margin of impedance intersection is studied. As shown in Fig. 23, the phase margin becomes the maximum value when f_c is equal to 154Hz.

Based on the analysis above, the maximum phase margin of impedance intersection could be obtained when the optimal parameters of QPR controller ($k_r = 0.22$ and $\omega_c = 2\pi \times 154$) are selected.

4) SIMULATION RESULTS

The impedance including stabilization control strategy with the optimal controller parameters is shown in Fig. 24 (a). In addition to the intersections near the oscillation frequency, there is also an intersection at 116 Hz, but the phase margin of this intersection point is large enough, and there is no risk of oscillation. Comparing the impedances with and without stabilization control strategy, it is obvious that the impedance around oscillation frequency has been improved a lot. As shown in Fig. 24(b), as the system added a stabilization control strategy, the impedance intersection changed from 888Hz to 879Hz, and the phase margin increased from 0.8° to 28.4°, which provides sufficient stability margin for the system.

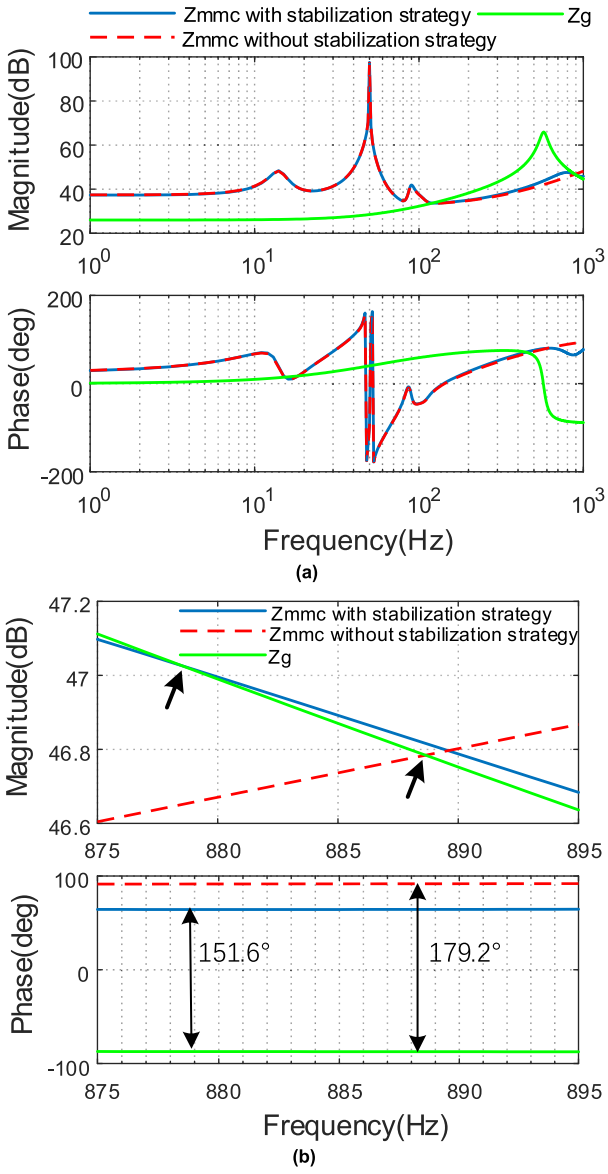

FIGURE 24. Comparison of impedance with/without stabilization control strategy. (a)Full scale, (b)Zoomed-in Figure.

In order to verify the correctness of the above analysis, the stabilization control strategy is added to the control system for simulation. As shown in Fig. 25, the stabilization control strategy is enabled at 2.04s, the oscillation harmonics of phase *a* voltage and current are quickly suppressed, the voltage and current waveforms are improved to a basically ideal sinusoidal wave after 0.02s, the system no longer oscillates any more. The total THD of current decreases from 14% (as shown in Fig. 18) to 0.09% which meet engineering requirements, proving that the oscillations have been mitigated effectively. This proves the effectiveness of the stabilization control strategy proposed in this article and the rationality of the optimal design of the stability strategy parameters.

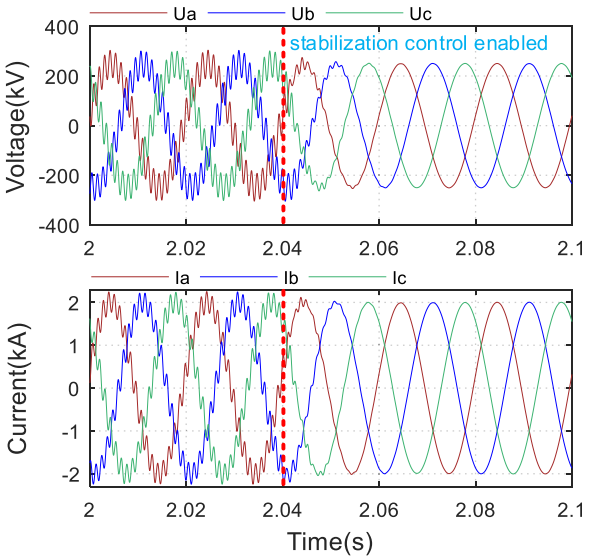

FIGURE 25. MMC terminal voltage and output current simulation when stabilization control strategy is enabled.

VI. CONCLUSION

Mechanism of high-frequency oscillation in MMC-HVDC which is caused by time delay is analyzed by impedance-based stability criterion in this article. Firstly, the MMC impedance is modeled considering complete control loops, including power outer loop, current control loop, circulating-current control loop, PLL and especially the time delay. In the meanwhile, this article pointed out that the high-frequency negative damping of impedance is brought by the time delay, which is the core cause of the system oscillation. Then, a stabilization control strategy is proposed to suppress the system oscillation. In addition, impedance considering this stabilization control strategy is also modeled and the parameters of this stability strategy are optimized to achieve maximum phase margin of the interconnected system. Finally, the simulation results demonstrate the correctness of oscillation mechanism analysis and effectiveness of proposed stabilization control strategy.

The main conclusions are as follows.

1) The outer-loop control mainly affects the impedance characteristics of MMC in the low-frequency area.

2) Time delay affects the impedance characteristics of MMC in the high-frequency area, and lead to a negative damping which is very harmful to system stability.

3) The stabilization control strategy should be considered during impedance modeling process to analyze the detailed influence on system stability.

In summary, time delay is a key factor in system oscillation and should be considered. The impedance-based parameters optimization method for stabilization control strategy proposed in this article can also be used in other system stabilization strategies.

REFERENCES

[1] S. P. Teeuwsen, "Modeling the trans bay cable project as voltage-sourced converter with modular multilevel converter design," in *Proc. IEEE Power Energy Soc. Gen. Meeting*, Detroit, MI, USA, Jul. 2011, pp. 1–8.
[2] F. Deng and Z. Chen, "Voltage-balancing method for modular multilevel converters switched at grid frequency," *IEEE Trans. Ind. Electron.*, vol. 62, no. 5, pp. 2835–2847, May 2015.
[3] L. Xiong, F. Zhuo, X. Liu, Z. Xu, and Y. Zhu, "Fault-tolerant control of CPS-PWM-based cascaded multilevel inverter with faulty units," *IEEE J. Emerg. Sel. Topics Power Electron.*, vol. 7, no. 4, pp. 2486–2497, Dec. 2019.
[4] L. Xiong, X. Liu, C. Zhao, and F. Zhuo, "A fast and robust real-time detection algorithm of decaying DC transient and harmonic components in three-phase systems," *IEEE Trans. Power Electron.*, vol. 35, no. 4, pp. 3332–3336, Apr. 2020.
[5] J. Lyu, X. Cai, and M. Molinas, "Optimal design of controller parameters for improving the stability of MMC-HVDC for wind farm integration," *IEEE J. Emerg. Sel. Topics Power Electron.*, vol. 6, no. 1, pp. 40–53, Mar. 2018.
[6] C. Buchhagen, M. Greve, A. Menze, and J. Jung, "Harmonic stability-practical experience of a TSO," in *Proc. Wind Integr. Workshop*, Vienna, Austria, Nov. 2016, pp. 1–6.
[7] C. Zou, H. Rao, S. Xu, Y. Li, W. Li, J. Chen, X. Zhao, Y. Yang, and B. Lei, "Analysis of resonance between a VSC-HVDC converter and the AC grid," *IEEE Trans. Power Electron.*, vol. 33, no. 12, pp. 10157–10168, Dec. 2018.
[8] J. Sun, "Impedance-based stability criterion for grid-connected inverters," *IEEE Trans. Power Electron.*, vol. 26, no. 11, pp. 3075–3078, Nov. 2011.
[9] J. Sun and H. Liu, "Sequence impedance modeling of modular multilevel converters," *IEEE J. Emerg. Sel. Topics Power Electron.*, vol. 5, no. 4, pp. 1427–1443, Dec. 2017.
[10] D. C. Ludois and G. Venkataramanan, "Simplified terminal behavioral model for a modular multilevel converter," *IEEE Trans. Power Electron.*, vol. 29, no. 4, pp. 1622–1631, Apr. 2014.
[11] G. Bergna Diaz, J. A. Suul, and S. D'Arco, "Small-signal state-space modeling of modular multilevel converters for system stability analysis," in *Proc. IEEE Energy Convers. Congr. Expo. (ECCE)*, Montreal, QC, Canada, Sep. 2015, pp. 5822–5829.
[12] N.-T. Trinh, M. Zeller, K. Wuerflinger, and I. Erlich, "Generic model of MMC-VSC-HVDC for interaction study with AC power system," *IEEE Trans. Power Syst.*, vol. 31, no. 1, pp. 27–34, Jan. 2016.
[13] Y. Li, G. Tang, J. Ge, Z. He, H. Pang, J. Yang, and Y. Wu, "Modeling and damping control of modular multilevel converter based DC grid," *IEEE Trans. Power Syst.*, vol. 33, no. 1, pp. 723–735, Jun. 2018.
[14] J. Lyu, X. Cai, and M. Molinas, "Frequency domain stability analysis of MMC-based HVdc for wind farm integration," *IEEE J. Emerg. Sel. Topics Power Electron.*, vol. 4, no. 1, pp. 141–151, Mar. 2016.
[15] J. Lyu, X. Zhang, X. Cai, and M. Molinas, "Harmonic state-space based small-signal impedance modeling of a modular multilevel converter with consideration of internal harmonic dynamics," *IEEE Trans. Power Electron.*, vol. 34, no. 3, pp. 2134–2148, Mar. 2019.
[16] S. G. Parker, B. P. McGrath, and D. G. Holmes, "Regions of active damping control for LCL filters," *IEEE Trans. Ind. Appl.*, vol. 50, no. 1, pp. 424–432, Jan. 2014.
[17] X. Zhang, J. W. Spencer, and J. M. Guerrero, "Small-signal modeling of digitally controlled grid-connected inverters with *LCL* filters," *IEEE Trans. Ind. Electron.*, vol. 60, no. 9, pp. 3752–3765, Sep. 2013.
[18] Y. Tu, J. Liu, Z. Liu, D. Xue, and L. Cheng, "Impedance-based analysis of digital control delay in grid-tied voltage source inverters," *IEEE Trans. Power Electron.*, vol. 35, no. 11, pp. 11666–11681, Nov. 2020, doi: 10.1109/TPEL.2020.2987198.
[19] J. Sun, I. Vieto, E. V. Larsen, and C. Buchhagen, "Impedance-based characterization of digital control delay and its effects on system stability," in *Proc. 20th Workshop Control Modeling Power Electron. (COMPEL)*, Toronto, ON, Canada, Jun. 2019, pp. 1–8.
[20] Z. Li, Z. Wang, Y. Wang, T. Yin, N. Mei, B. Yue, and W. Lei, "Accurate impedance modeling and control strategy for improving the stability of DC system in multiterminal MMC-based DC grid," *IEEE Trans. Power Electron.*, vol. 35, no. 10, pp. 10026–10049, Oct. 2020, doi: 10.1109/TPEL.2020.2975619.
[21] D. Xu, M. Han, and A. M. Gole, "Propagation of AC background harmonics in MMC HVdc multiterminal systems due to resonances and mitigation measures," *IEEE Trans. Power Del.*, vol. 33, no. 1, pp. 229–238, Feb. 2018.
[22] T. Jiao, W. X. Zheng, and S. Xu, "Unified stability criteria of random nonlinear time-varying impulsive switched systems," *IEEE Trans. Circuits Syst. I, Reg. Papers*, early access, Apr. 20, 2020, doi: 10.1109/TCSI.2020.2983324.
[23] G. Zong, W. Qi, and H. R. Karimi, "L_1 control of positive semi-Markov jump systems with state delay," *IEEE Trans. Syst., Man, Cybern. Syst.*, early access, Mar. 24, 2020, doi: 10.1109/TSMC.2020.2980034.
[24] H. Ren, G. Zong, and H. R. Karimi, "Asynchronous finite-time filtering of networked switched systems and its application: An event-driven method," *IEEE Trans. Circuits Syst. I, Reg. Papers*, vol. 66, no. 1, pp. 391–402, Jan. 2019, doi: 10.1109/TCSI.2018.2857771.
[25] L. Harnefors, A. Antonopoulos, S. Norrga, L. Angquist, and H.-P. Nee, "Dynamic analysis of modular multilevel converters," *IEEE Trans. Ind. Electron.*, vol. 60, no. 7, pp. 2526–2537, Jul. 2013.
[26] K. Ilves, A. Antonopoulos, S. Norrga, and H.-P. Nee, "Steady-state analysis of interaction between harmonic components of arm and line quantities of modular multilevel converters," *IEEE Trans. Power Electron.*, vol. 27, no. 1, pp. 57–68, Jan. 2012.
[27] M. Beza, M. Bongiorno, and G. Stamatiou, "Analytical derivation of the AC-side input admittance of a modular multilevel converter with Open- and closed-loop control strategies," *IEEE Trans. Power Del.*, vol. 33, no. 1, pp. 248–256, Feb. 2018.
[28] J. Lyu, Q. Chen, and X. Cai, "Impedance modeling of modular multilevel converters by harmonic linearization," in *Proc. IEEE 17th Workshop Control Modeling Power Electron. (COMPEL)*, Trondheim, Norway, Jun. 2016, pp. 1–6.
[29] J. R. C. Orillaza and A. R. Wood, "Harmonic state-space model of a controlled TCR," *IEEE Trans. Power Del.*, vol. 28, no. 1, pp. 197–205, Jan. 2013.
[30] J. Khazaei, M. Beza, and M. Bongiorno, "Impedance analysis of modular multi-level converters connected to weak AC grids," *IEEE Trans. Power Syst.*, vol. 33, no. 4, pp. 4015–4025, Jul. 2018.
[31] H. Wu, X. Wang, L. Kocewiak, and L. Harnefors, "AC impedance modeling of modular multilevel converters and two-level voltage-source converters: Similarities and differences," in *Proc. IEEE 19th Workshop Control Modeling Power Electron. (COMPEL)*, Padua, Italy, Jun. 2018, pp. 1–8.
[32] K. Ji, G. Tang, J. Yang, Y. Li, and D. Liu, "Harmonic stability analysis of MMC-based DC system using DC impedance model," *IEEE J. Emerg. Sel. Topics Power Electron.*, vol. 8, no. 2, pp. 1152–1163, Jun. 2020.
[33] F. Zhao, G. Xiao, and T. Zhao, "Accurate steady-state mathematical models of arm and line harmonic characteristics for modular multilevel converter," *IEEE Trans. Power Del.*, vol. 33, no. 3, pp. 1308–1318, Jun. 2018.
[34] K. Ji, G. Tang, H. Pang, and J. Yang, "Impedance modeling and analysis of MMC-HVDC for offshore wind farm integration," *IEEE Trans. Power Del.*, vol. 35, no. 3, pp. 1488–1501, Jun. 2020.
[35] J. Sun and H. Liu, "Impedance modeling and analysis of modular multilevel converters," in *Proc. IEEE 17th Workshop Control Modeling Power Electron. (COMPEL)*, Trondheim, Norway, Jun. 2016, pp. 1–9.

TAIYUAN YIN (Student Member, IEEE) is currently pursuing the Ph.D. degree in electrical engineering from Xi'an Jiao Tong University, Xi'an, China.

His current interests include modeling and control of modular multilevel converter and stability analysis of MMC-based HVDC systems.

YUE WANG (Member, IEEE) was born in Liaoning, China, in 1972. He received the B.S. degree from Xi'an Jiaotong University, Xi'an, China, in 1994, the M.S. degree from Beijing Jiaotong University, Beijing, China, in 2000, and the Ph.D. degree from Xi'an Jiaotong University, in 2003, all in electrical engineering.

He is currently a Full Professor with the School of Electrical Engineering, Xi'an Jiaotong University. His research interests include wireless power transfer, active power filters, multilevel converters, and HVDC.

BO YUE was born in Shaanxi, China, in 1976. He received the Ph.D. degree in electrical engineering from Xi'an Jiaotong University, Xi'an, China, in 2003.

He is currently a Senior Engineer with the State Grid Economic and Technological Research Institute Company Ltd. His main research interests include HVDC and high-voltage technology.

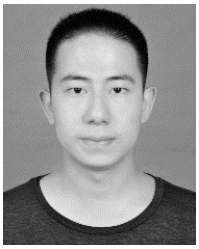

PENGFAN XU was born in Hebei, China, in 1994. He received the B.S. degree in electrical engineering from the University of Electronic Science and Technology of China, Chengdu, China, in 2017, and the M.S. degree in electrical engineering from Xi'an Jiaotong University, in 2020.

His main research interests include modeling and control of multilevel converters, and HVDC.

PENGKUN LI received the B.S. degree in electrical engineering from Beijing Jiaotong University, Beijing, China, in 2017. He is currently pursuing the Ph.D. degree with Xi'an Jiaotong University, Xi'an, China.

His research interests include modeling, control, and small-signal stability analysis of multilevel converters.

NIAN MEI was born in Hubei, China, in 1982. She received the Ph.D. degree in electrical engineering from the Huazhong University of Science and Technology, Wuhan, China, in 2009.

She is currently a Senior Engineer with the State Grid Economic and Technological Research Institute Company Ltd. Her main research interests include voltage source converter-based HVDC and line commutated converter-based HVDC.

DONG XU received the B.Eng. degree from the North China Electric Power University, Beijing, China, in 2012, where he is currently pursuing the Ph.D. degree. From October 2015 to October 2016, he was a Visiting Scholar with the University of Manitoba, Canada. He is currently an Engineer with the State Grid Economic and Technological Research Institute Company Ltd. His research interests include the modeling, control, and simulation of HVDC systems.